Earth and Planetary Science Letters 361 (2013) 58–63

Contents lists available at SciVerse ScienceDirect

Earth and Planetary Science Letters

journal homepage: www.elsevier.com/locate/epsl

Thermodynamics of the $MgO–SiO_2$ liquid system in Earth's lowermost mantle from first principles

Nico de Koker [a,b,*], Bijaya B. Karki [c,d], Lars Stixrude [e]

[a] Bayerisches Geoinstitut, Universität Bayreuth, D-95440 Bayreuth, Germany
[b] School of Geosciences, University of the Witwatersrand, Private Bag 3, 2050, Wits, South Africa
[c] Department of Computer Science, Louisiana State University, Baton Rouge, LA 70803, United States
[d] Department of Geology and Geophysics, Louisiana State University, Baton Rouge, LA 70803, United States
[e] Department of Earth Sciences, University College London, Gower Street, London, WC1E 6BT, United Kingdom

ARTICLE INFO

Article history:
Received 8 September 2012
Received in revised form
12 November 2012
Accepted 15 November 2012
Editor: T. Spohn
Available online 14 December 2012

Keywords:
Earth's mantle
silicate melts
high pressure melting
origin of Earth
core–mantle boundary

ABSTRACT

Knowledge of the multi-component thermodynamics and phase equilibria of silicate melts in Earth's deep interior are key to understanding the thermal and chemical evolution of the planet, yet the melting phase diagram of the lower mantle remains poorly constrained, with large uncertainties in both eutectic composition and temperature. We use results from first-principles molecular dynamics of nine compositions along the $MgO–SiO_2$ binary to investigate the compositional dependence of liquid state thermodynamics, applying our results to describe incongruent melting for the system at deep lower mantle pressures. Our phase diagram is bi-eutectic throughout the lower mantle, with no liquid immiscibility. Accounting for solid–liquid partitioning of Fe, we find partial melts of basaltic and peridotitic lithologies to be gravitationally stable at the core–mantle boundary, while liquidus density contrasts predict that perovskite will sink and periclase will float in a crystallizing pyrolytic magma ocean.

1. Introduction

Melting at high pressure is a ubiquitous process in the formation and evolution of terrestrial planets. The moon forming giant impact alone would have melted the entire Earth (Canup, 2004; Ke and Solomatov, 2006), while seismic ultra-low velocity zones atop the core–mantle boundary (CMB) are often associated with patches of partial melt (Williams and Garnero, 1996). As the vector of chemical differentiation during magma ocean crystallization and melting of the solid mantle, the buoyancy contrast between liquid and solid phases is a critical factor in planetary dynamics and evolution. These contrasts can differ notably among mineral phases, so that the crystallization sequence is just as important for understanding these processes. Most models describing crystallization of a magma ocean assume perovskite to be the liquidus phase, with crystallization starting from the base and crystals forming at shallower depths sinking to the bottom (Solomatov, 2007).

Very little data on incongruent melting at lower mantle pressures is available to test these assumptions. Indeed, high pressure experiments indicate that the sequence of crystallization depends on pressure (Fiquet, 2010), while it was recently shown that the adiabatic thermal gradient in a magma ocean will be notably steeper than previously thought (Mosenfelder et al., 2007; Stixrude and Karki, 2005), so that crystallization may in fact initiate at depths shallower than the base (Stixrude et al., 2009). High pressure studies of congruent melting indicate that the Clapeyron slope of melting for MgO is likely higher than that of $MgSiO_3$ perovskite, which could potentially result in a strong pressure dependence in the $MgO–MgSiO_3$ eutectic composition.

The ambient pressure $MgO–SiO_2$ phase diagram, first mapped out by Bowen and Andersen (1914), suggests a number of intriguing questions regarding potential high pressure phenomena. The system exhibits liquid immiscibility in high-silica compositions (Hageman and Oonk, 1986), a very large contrast between the liquidus temperatures at intermediate (geological) compositions and MgO (Riley, 1966), a eutectic between MgO periclase and $MgSiO_4$ forsterite, another eutectic between $MgSiO_3$ enstatite and SiO_2 cristobalite, and a peritectic by which enstatite melts into a slightly more SiO_2-rich liquid phase co-existing with forsterite.

Low pressure liquid immiscibility, notably also observed in the $CaO–SiO_2$ (Hageman and Oonk, 1986) and $FeO–SiO_2$ (Bowen and Schairer, 1935) systems, has been shown to vanish by around 5 GPa (Dalton and Presnall, 1997). If this phenomenon reappears at lower mantle pressures, an idea as yet untested by experiment

* Corresponding author. Tel.: +27 11 717 6547.
E-mail address: ndekoker@gmail.com (N. de Koker).

0012-821X/$ - see front matter
http://dx.doi.org/10.1016/j.epsl.2012.11.026

or simulation, the geochemical evolution of a cooling magma ocean, and subsequently the mantle, would be significantly more complex than current models assume.

Description of incongruent melting in the deep mantle requires knowledge of the liquid Gibbs free energy as a function not only of pressure and temperature, but also of composition, $G(P,T,X)$. Numerous studies have considered congruent melting of mantle phases, thus implicitly taking account of $G(P,T)$, but our knowledge of the behavior of liquid free energy with composition at deep mantle pressures remains sparse. Some clues to the nature of $G(X)$ are obtained from comparisons between measurements of shock compressed liquid volume (Asimow and Ahrens, 2010), and studies of the crystallization sequence at deep mantle conditions (Fiquet, 2010; Ito et al., 2004).

Here we use first-principles molecular dynamics (FPMD) to describe the thermodynamics of mixing in the MgO–SiO_2 system, and subsequently derive the chemical potential for the system. We apply this description to constrain incongruent melting equilibria for the lower mantle.

2. Theory

FPMD has proven to be a powerful and robust tool for investigating silicate melts at extreme pressures, reliably reproducing shock compression data to very high pressures and temperatures (de Koker, 2010; de Koker and Stixrude, 2009; Sun, 2011). Our simulation approach has been discussed extensively in our previous work (de Koker, 2010; de Koker et al., 2008; Stixrude and Karki, 2005). Density functional theory (DFT; Hohenberg and Kohn, 1964; Kohn and Sham, 1965) implemented in the VASP plane-wave code (Kresse and Furthmüller, 1996) is used to perform *NVT*-ensemble first-principles molecular dynamics (FPMD), with ultra-soft pseudopotentials (Kresse and Hafner, 1994) and the local density approximation (LDA). We combine existing simulation results for liquid MgO (de Koker and Stixrude, 2009; Karki et al., 2006), Mg_2SiO_4 (de Koker et al., 2008), $MgSiO_3$ (de Koker and Stixrude, 2009; Stixrude and Karki, 2005) and SiO_2 (Karki et al., 2007), together with MgO periclase (de Koker and Stixrude, 2009), $MgSiO_3$ perovskite (de Koker and Stixrude, 2009; Stixrude and Karki, 2005), and SiO_2 stishovite (Karki et al., 2007), with new simulations for liquids of intermediate composition: Mg_5SiO_7, $Mg_3Si_2O_7$, $MgSi_2O_5$, $MgSi_3O_7$ and $MgSi_5O_{11}$. More details on these simulations are given in the online supplement.

We fit an updated version of the fundamental thermodynamic relation of de Koker and Stixrude (2009) to the simulation results to obtain a thermodynamic model $G(P,T)$ for each composition considered, and combine these to construct a single representation of $G(P,T,X)$ in the system. These thermodynamic interpolation formulae are specified in the online supplement.

3. Results

3.1. Thermodynamics of mixing

Multi-component thermodynamics is expressed through the comparison of model values obtained for each simulated intermediate composition to the oxide end-members. Values of the enthalpy of mixing (H_{mix}) show positive values for silica rich compositions at low pressure. As pressure increases, values become negative and increasingly independent of pressure (Fig. 1). H_{mix} values are consistent with observed immiscibility at ambient pressure (Hageman and Oonk, 1986), as well as its disappearance by 5 GPa (Dalton and Presnall, 1997).

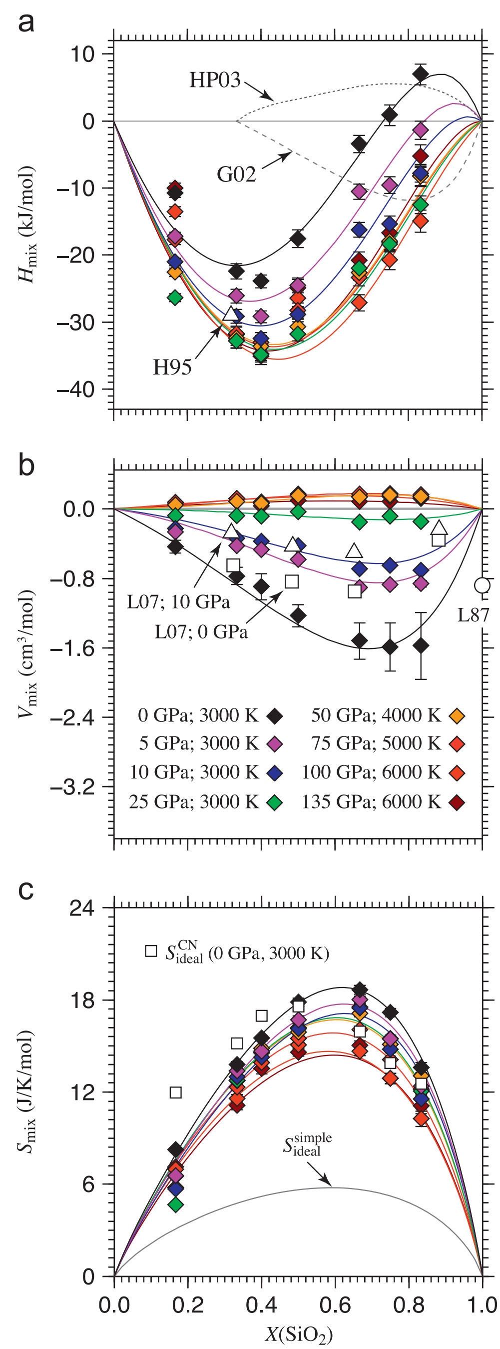

Fig. 1. (a) Enthalpy, (b) volume and (c) entropy of mixing. Diamonds – values computed using the individual thermodynamic models for each simulated composition; lines – model values determined from $G(P,T,X)$ (Eq. (2)). Change of S_{mix} with pressure is constrained from H_{mix} through Eq. (1); S_{mix} at ambient pressure is constrained from phase equilibria (refer to online supplement), and existing estimates at MgO, Mg_2SiO_4, $MgSiO_3$ and SiO_2. S_{mix} is higher than the configurational value for mixing of the endmembers (MgO, SiO_2; $S_{ideal}^{\mathrm{simple}} = Nk_{\mathrm{B}} \sum X \ln X$; Ghiorso et al., 2002), yet comparable to configurational values determined from the distribution of Mg and Si coordination species, $S_{ideal}^{\mathrm{CN}} = Nk_{\mathrm{B}} \sum_{ij} y_{ij} \ln y_{ij}$, where y_{ij} denotes the fraction of cations of type i (Mg or Si) in coordination state j (de Koker et al., 2008). Units in mol of oxides; H95—H_{mix} based on combining solid enthalpies of mixing and fusion (Hess, 1995); HP03—H_{mix} values determined by Holland and Powell (2003) based on phase equilibria; G02—H_{mix} from extrapolating multi-component parameterization of Ghiorso et al. (2002); L87—the experimental partial molar V of SiO_2 (Lange and Carmichael, 1987); L07—V_{mix} results obtained by Lacks et al. (2007) using empirical potentials. (For interpretation of the references to color in this figure, the reader is referred to the web version of this article.)

The volume of mixing (V_{mix}) becomes increasingly ideal at elevated pressure. Indeed, V_{mix} is essentially zero over most of the lower mantle, consistent with shock compression results (Asimow and Ahrens, 2010). Negative volumes of mixing seen at ambient pressure highlight the fact that applying constant partial molar volumes to a large compositional range must be done with caution (Ghiorso et al., 2002; Lange and Carmichael, 1987).

Together, V_{mix} and the pressure dependence of H_{mix} constrain the pressure dependence of the entropy of mixing S_{mix} through

$$T\left(\frac{\partial S_{mix}}{\partial P}\right)_T = \left(\frac{\partial H_{mix}}{\partial P}\right)_T - V_{mix} \quad (1)$$

S_{mix} itself is determined by integrating Eq. (1), with the integration constant fixed by matching to experimental phase equilibria at ambient pressure (refer to online supplement). The variation of S_{mix} with pressure relative to this fixed point is fully constrained by our FPMD results.

We find that prominent liquid immiscibility at low pressure in the MgO–SiO_2 system, known to vanish with increasing pressure, remains absent throughout the lower mantle. The increasingly linear nature of mixing of volume and enthalpy as pressure increases is consistent with results from shock compression of liquid silicates, although these experiments were conducted in somewhat different compositions over a notably smaller variations of silica contents (Asimow and Ahrens, 2010).

We fit the excess Gibbs free energy of mixing using an asymmetric regular solution model (Haselton and Newton, 1980; Thompson Jr., 1967)

$$G_{mix} = G_{ideal} + W_A Y^2(1-Y) + W_B Y(1-Y)^2, \quad (2)$$

with W_i interaction parameters, and $Y = X/[X+\lambda(1-X)]$, so that $Y=X$ when $\lambda=1$, and $\lambda \neq 1$ allows for additional asymmetry in G_{mix}. Taking $X = X(SiO_2)$, our low pressure enthalpy of mixing results require $\lambda=1.43$. Previous studies of thermodynamics of mixing in silicate systems have also suggested $\lambda \neq 1$ (Burnham, 1975; Hess, 1995; Zhou and Miller, 1997). Although more complex and ostensibly more physical models have been developed, we choose (2) for its simplicity, continuity, and the empirical fact that it works very well in representing our FPMD results. We note that some previous studies have interpreted values of λ different from unity in terms of the compositions of complexes that are mixing, for example Si_2O_4 instead of SiO_2, or Mg_2O_2 instead of MgO (Hess, 1995). However, we find no simple relationship between the value of λ required to match our FPMD results and the liquid structures observed in our simulations, which contain multiple species at all temperatures (de Koker, 2010; de Koker et al., 2008; Stixrude and Karki, 2005) that change with compression.

With G_{mix} constrained, we can derive all other thermodynamic properties at any composition along the join, including H, V, S, (Fig. 1) and the chemical potential μ,

$$\mu_A = \frac{\partial G}{\partial X_A} \quad (3)$$

3.2. High pressure MgO–SiO_2 phase diagram

We find that the MgO–SiO_2 phase diagram at lower mantle conditions is bi-eutectic (Fig. 2). The compositions of the two eutectic points vary only weakly with pressure, corresponding closely to values characteristic of peridotite and basalt, respectively. The periclase-perovskite eutectic shifts by about 2 mol % towards MgO between 25 and 60 GPa, consistent with experimental observations (Fiquet, 2010; Ito et al., 2004). For a peridotitic magma ocean, this signals a change in the liquidus phase from periclase at shallow depths to perovskite at greater depth, with the position of the transition depending sensitively on composition.

Solidus temperatures for the MgO–SiO_2 system at the base of Earth's mantle (136 GPa) are 4930 ± 170 K and 4580 ± 210 K for $X < 0.5$ and $X > 0.5$, respectively. Based on scaling arguments, we estimate that replacement of 10 mol% MgO by FeO (Mg#=90) will lower the periclase-perovskite solidus temperature by 180–320 K; for Mg#=80, representative of basaltic oceanic crust, the silica–perovskite solidus will be decreased by a similar amount. These estimates are determined by adjusting the chemical potential of liquid and solid for a given FeO concentration (refer to online supplement), using $K_{MF} = 0.40 \pm 0.15$ as an estimate of the partition coefficient between solid and melt (Trønnes and Frost, 2002). The theoretical basis for this adjustment in the chemical potential is explained in detail in section S4 of the online supplement.

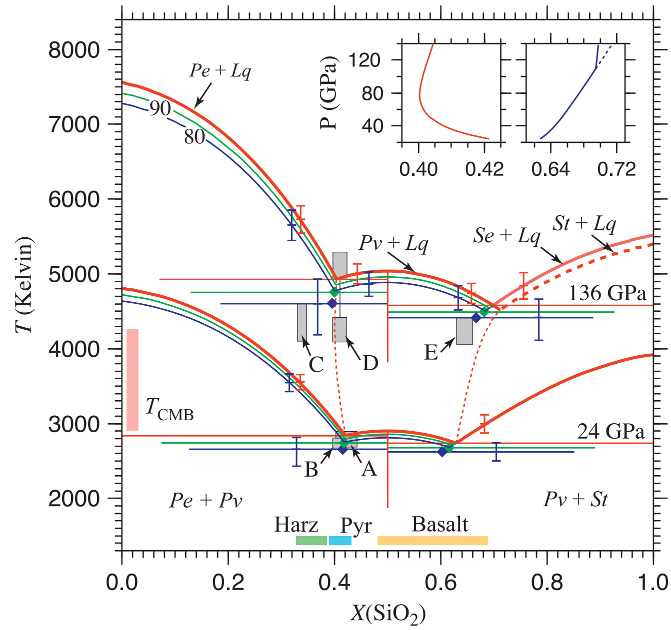

Fig. 2. Melting phase diagram for the MgO–SiO_2 system in the lower mantle (heavy red lines). Thinner green and blue lines indicate liquidi adjusted for indicated Mg# values (refer to online supplement); diamonds indicate the corresponding solidus points on the cotectic. Error bars represent uncertainty due to FPMD simulations and the partition coefficient used in adjusting for Fe (Trønnes and Frost, 2002). Stishovite metastability above 40 GPa is negligible in the $CaCl_2$-structure stability field, with the change to seifertite above 110 GPa (Oganov et al., 2005) resulting in a small increase in melting temperature (pink line, determined using the Clapeyron relation). Experimental measurements are shown by grey boxes; at 24 GPa, (A) MgO–SiO_2 eutectic (Presnall et al., 1998), (B) peridotite eutectic (Ito et al., 2004); at 136 GPa, (C) shock melting of Fo90 (Holland and Ahrens, 1997), (D) peridotite solidus and liquidus (Fiquet, 2010), (E) extrapolated high P melting of MORB (Hirose et al., 1999). Pe—periclase, Se—seifertite, St—stishovite, Pv—perovskite, Lq—liquid, Harz—harzburgite, Pyr—pyrolite. Inset: Variation of Pe–Pv (red, left) and Pv–St (blue, right) eutectic compositions with pressure. Depending on the composition of a peridotitic magma ocean, Pe or Pv will be the liquidus phase at different depths in the mantle. (For interpretation of the references to color in this figure legend, the reader is referred to the web version of this article.)

3.3. Liquid structure as a function of composition

Structural adjustment in response to compression is most readily expressed in terms of the coordination of O around Si atoms, Z_{Si-O}, while the nature and extent of polymerization is best considered through Z_{O-Si}, the coordination of Si around O atoms. Coordination numbers are computed as the appropriately normalized area under the first peak of the radial distribution function (de Koker et al., 2008; McQuarrie, 1984). Z_{O-Si} values of intermediate compositions vary continuously along the binary, with multiple O-coordination species present at each composition (Fig. 3). For a given degree of compression relative to the volume at ambient pressure, Z_{Si-O} values do not vary notably along the binary, but do

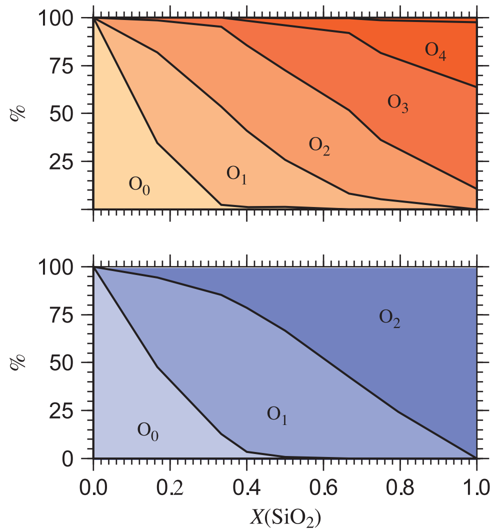

Fig. 3. The distribution of oxygen species at 6000 K and 136 GPa (top), and 3000 K and 0 GPa (bottom). O_F–$Z_{O-Si}=0$, O_N–$Z_{O-Si}=1$, O_B–$Z_{O-Si}=2$, O_3–$Z_{O-Si}=3$, O_4–$Z_{O-Si}=4$.

show a stark contrast with pure SiO_2 (Fig. 4a). Z_{Si-O} increases uniformly from 4 to 6 over a two-fold compression range relative to V_0, the volume at 0 GPa and 3000 K, i.e. $V/V_0=1.0$ to $V/V_0=0.5$. However in pure SiO_2 compression is initially accommodated by an increase in the mean framework ring-size (Karki et al., 2007; Stixrude and Bukowinski, 1990), with coordination change becoming the primary compression mechanism around $V/V_0=0.8$ ($\sim$4 GPa, depending on T), from where coordination changes dominate strongly.

The changes in liquid structure with pressure and composition are strongly reflected by the thermodynamic properties. The Grüneisen parameter (γ) increases with compression for all liquids along the join, albeit delayed in SiO_2, and highlights the relation between γ and Z_{Si-O} (Fig. 4b). In solids, high pressure phase transitions involving an increase in Z_{Si-O} result in notable increases in γ, with similar effects predicted for other cations, including Mg^{2+} (Jeanloz and Roufosse, 1982). The increase of γ with MgO content, and its notably weaker volume dependence in MgO suggests that Mg–O bonds have intrinsically higher γ values, less sensitive to changes in bond length. Density decreases with increasing silica content at low pressure, but increases with increasing silica content at high pressure. The greater compressibility at the silica rich end is consistent with the collapse of the initially open framework structure for silica rich compositions and is reflected in the decrease of the values of the reference bulk modulus K_0 from 24 GPa in the Mg-rich compositions to 12.5 GPa in silica-rich compositions. This decrease in bulk modulus is accompanied by an increase in K_0' from $\sim$5.6 to $\sim$6.5 (Table 1), consistent with the K_0–K_0' anti-correlation observed in silicate liquids (Lange, 2007) Fig. 5.

The differences in compressibility and partial molar volume at different compositions are also reflected in the disappearance of liquid immiscibility with pressure. Liquid immiscibility is often ascribed to the Coulombic effects (Hudon and Baker, 2002; McGahay and Tomozawa, 1989), by which the small size and high charge of the Mg^{+2} ion is difficult to accommodate in the high SiO_2 compositions, resulting in energetically less favorable structures in the liquid with increased internal energy values (Hudon and Baker, 2002). However, the volumetric advantage of a single phase assemblage grows dominant with pressure, so that two less dense liquid phases has a higher enthalpy than a single dense phase with somewhat unfavorable structural species.

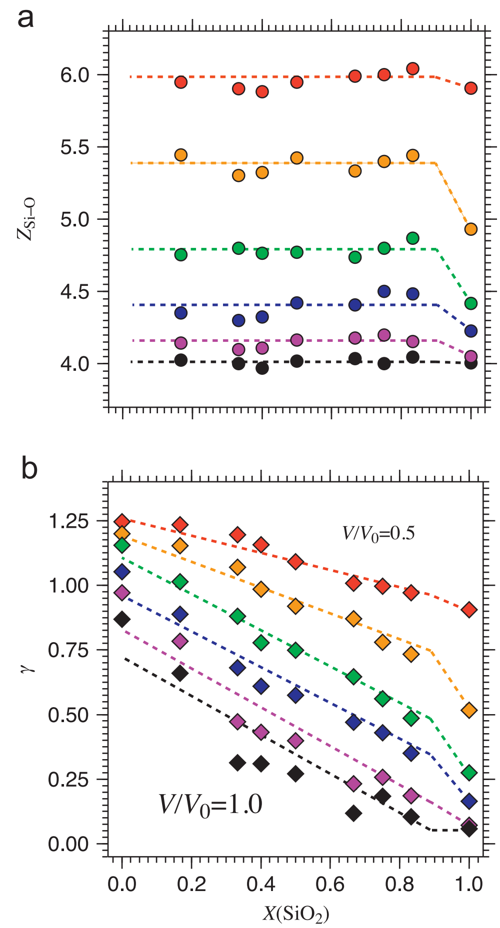

Fig. 4. (a) Silicon coordination Z_{Si-O} increases from 4 to 6 for all species considered upon two fold compression relative to V_0, the volume at 0 GPa and 3000 K as. determined from fitting the equation of state along the join. However the increase is notably delayed in SiO_2. (b) The Grüneisen parameter γ for all liquids on the join increases with compression and MgO content. The delay in its increase for SiO_2 reflects the delayed increase in Z_{Si-O}. T increases from 3000 K at V_0 to 6000 K at $0.5V_0$. Note that here individual colors denote degrees of compression: red—$0.5V_0$, yellow—$0.6V_0$, green—$0.7V_0$, blue—$0.8V_0$, magenta—$0.9V_0$, black—$1.0V_0$. (For interpretation of the references to color in this figure legend, the reader is referred to the web version of this article.)

Therefore, immiscibility arising due to similar structural accommodation problems is unlikely to arise in liquids at high pressures.

4. Geophysical implications

The fact that the MgO–$MgSiO_3$ eutectic composition changes little over the entire lower mantle pressure range may at first seem a simple and unsurprising result. Yet the increasing contrast between congruent melting curves of MgO and $MgSiO_3$ has lead to large differences in speculated eutectic compositions (Boehler, 1996; Miller et al., 1991; Zhou and Miller, 1997). A high MgO melting temperature relative to $MgSiO_3$ could potentially even express itself as a peritectic, with $MgSiO_3$ melting incongruently into an SiO_2-rich liquid and MgO periclase as residuum. If the similarity of the eutectic composition to that of peridotite is not simply a coincidence, the fact that it does not change much as a function of pressure raises the enticing possibility that extrasolar planets with non-volatile bulk compositions similar to that of the sun could also have mantles that are Earth-like in composition.

Computed eutectic temperatures are similar to estimates of temperatures reached in the thermal boundary layer at the base

Table 1
Thermodynamic properties of liquids on the $MgO–SiO_2$ binary at 0 GPa and 3000 K.

	MgO	Mg_5SiO_7	Mg_2SiO_4	$Mg_3Si_2O_7$	$MgSiO_3$	$MgSi_2O_5$	$MgSi_3O_7$	$MgSi_5O_{11}$	SiO_2
V/V_0	16.46 (1)	107.50 (1)	58.40 (8)	100.50 (8)	41.8 (1)	67.50 (9)	93.50 (8)	146.00 (1)	27.8 (2)
K_T (GPa)	33.49 (5)	24.33 (2)	19.50 (9)	18.35 (4)	17.2 (1)	12.92 (6)	12.53 (6)	13.06 (5)	6.2 (3)
K_S (GPa)	41.75 (9)	29.49 (7)	20.70 (7)	19.55 (4)	18.1 (1)	13.10 (6)	12.96 (10)	13.20 (3)	6.2 (4)
K_T'	4.81	5.61	5.99	5.97	6.17	6.9	6.72	5.16	14.94
α (10^{-6} K^{-1})	95 (1)	107 (1)	65 (2)	71 (1)	65 (2)	40 (1)	63 (2)	35 (3)	39 (3)
S (J/mol K)[a]	174.1 (2)	1125.4 (5)	595.1 (3)	1010.8 (5)	415.3 (2)	641.1 (5)	859.3 (7)	1283.2 (17)	205.5 (5)
C_V (Nk_B)	3.6 (2)	3.9 (1)	4.1 (4)	4.2 (2)	4.2 (4)	4.5 (3)	4.4 (3)	4.5 (2)	4.6 (2)
C_P (Nk_B)	4.5 (3)	4.8 (2)	4.4 (5)	4.5 (3)	4.4 (4)	4.5 (4)	4.6 (4)	4.6 (3)	4.6 (2)
γ	0.87 (1)	0.66 (1)	0.31 (1)	0.31 (1)	0.27 (1)	0.12 (1)	0.18 (1)	0.10 (1)	0.06 (2)

[a] Based on entropy of mixing, anchored on Mg_2SiO_4 and SiO_2.

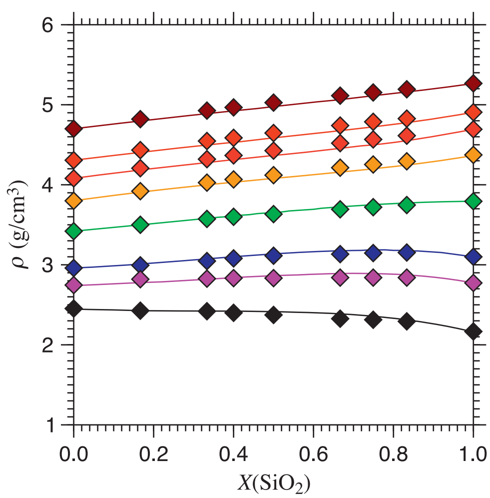

Fig. 5. Liquid density along lines of constant pressure along the $MgO–SiO_2$ join reveals the greater compressibility of high SiO_2 mixtures, with the compressibility of pure SiO_2 notably higher. Colors are coded as in Fig. 1, with lines obtained from the thermodynamic model. (For interpretation of the references to color in this figure legend, the reader is referred to the web version of this article.)

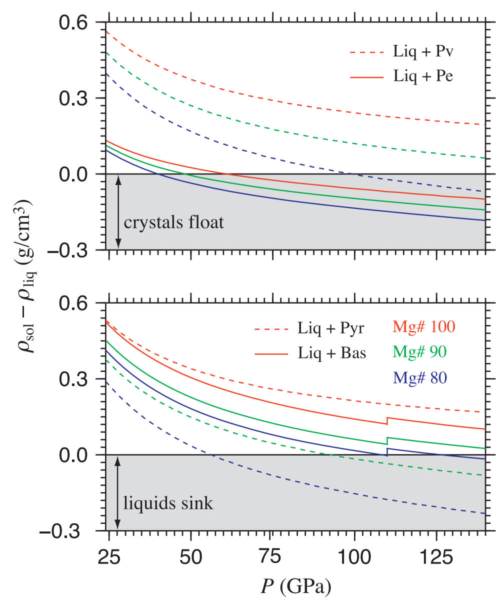

Fig. 6. (top) Density contrasts between solid and cotectic melt predicted during crystallization of a pyrolytic magma ocean. Note the opposing density contrasts of melt with perovskite (Pv) and periclase (Pe), and that a large degree of liquid fractionation is required for Pv to float. (bottom) Contrasts associated with melting indicate that partial melts of peridotitic (Pyr) and basaltic (Bas) lithologies will be gravitationally stable at the core–mantle boundary. Densities are computed at the corresponding eutectic temperatures.

of Earth's mantle (T_{CMB}), and after the likely decrease due to other chemical elements on the solidus are taken into account, consistent with the proposal that seismic ultra-low velocity zones represent regions of partially molten mantle (Labrosse et al., 2007; Williams and Garnero, 1996). Consistent with previous analyses (Zhou and Miller, 1997), we find that the solidus of enriched materials ($X>0.5$) is substantially less than that of primitive material, and will likely bracket the upper part of the range of estimates for T_{CMB}. The presence of relatively small scale enriched mantle heterogeneities may therefore explain the observation that ultra-low velocity zones are relatively localized (Williams and Garnero, 1996).

Analysis of solid-melt density contrasts indicate that partial melts of both basalt and peridotite will be gravitationally stable at the base of Earth's mantle. In the Fe-free system, liquids of eutectic composition are less dense than the isochemical solid aggregate, but inclusion of appropriate concentrations of Fe renders melts in both these systems negatively buoyant. These findings are consistent with previous analyses of the melting of perovskite (Stixrude and Karki, 2005), and are strengthened by recent indications that changes in spin state of Fe in silicate melts facilitates Fe partitioning into the liquid (Nomura et al., 2011).

Liquidus density contrasts relevant to a crystallizing pyrolytic magma ocean show that newly crystallized perovskite will sink, while periclase will float (Fig. 6). With perovskite enriched in incompatible elements relative to ferropericlase, this contrast can act as a vector for chemical differentiation. $CaSiO_3$ perovskite is about 4% denser than $MgSiO_3$ perovskite (Stixrude and Lithgow-Bertelloni, 2005), so that its additional affinity for incompatible elements will enhance this divergence; only after significant fractionation and enrichment of the liquid in iron will the remaining liquid phase be dense enough for perovskite to float.

The density contrast between crystal and liquid is a fundamental parameter controlling the process of crystal settling in a magma ocean. The fluid dynamics of this process are however still poorly understood and it is unclear to what extent slowly sinking crystals would gradually settle out or remain entrained in a the background flow (Solomatov, 2007). Stokes settling velocities determined from these density contrasts are between 10^{-2} and 10^{-6} m/s, depending on the crystal size and liquid viscosity (Karki and Stixrude, 2010; Martin and Nokes, 1989; Sparks et al., 1984), much smaller than plausible convective velocities associated with a vigorously convecting magma ocean.

5. Conclusions

First principles molecular dynamics simulations based on density functional theory is now capable of treating chemically rich systems with multiple stable phases and extensive solution. Our results on the $MgO–SiO_2$ join show bi-eutectic melting throughout the lower mantle with a slightly lower eutectic temperature on the enriched side. The eutectic compositions are remarkably stable with increasing pressure and correspond closely to basaltic and peridotitic bulk compositions. The simulations simultaneously and self-consistently predict the density contrast between co-existing liquid and crystals. At the mantle solidus, liquids are denser than co-existing solids, providing a plausible explanation for the origin of ultra-low velocity zones at the base of the mantle in terms of partial melt. At the magma ocean liquidus, crystal buoyancy varies with phase, with perovskites tending to sink and periclase tending to float. These results place important constraints on the presence of melt at the base of the present-day mantle and on the chemical evolution of the putative magma ocean.

Appendix A. Supplementary material

Supplementary data associated with this article can be found in the online version at http://dx.doi.org/10.1016/j.epsl.2012.11.026.

References

Asimow, P.D., Ahrens, T.J., 2010. Shock compression of liquid silicates to 125 GPa: the anorthite-diopside join. J. Geophys. Res. 115, B10209, http://dx.doi.org/10.1029/2009JB007145.

Boehler, R., 1996. Melting temperature of the Earth's mantle and core: Earth's thermal structure. Annu. Rev. Earth Planet. Sci. 24, 15–40.

Bowen, N.L., Andersen, O., 1914. The binary system $MgO–SiO_2$. Am. J. Sci. 37, 487–500.

Bowen, N.L., Schairer, J.F., 1935. The system, $MgO–FeO–SiO_2$. Am. J. Sci. 29, 151–217.

Canup, R.M., 2004. Simulations of a late lunar-forming impact. ICARUS 168, 433–456.

Dalton, J.A., Presnall, D.C., 1997. No liquid immiscibility in the system $MgSiO_3$–SiO_2 at 5.0 GPa. Geochim. Cosmochim. Acta 61, 2367–2373.

de Koker, N., 2010. Structure, thermodynamics, and diffusion in $CaAl_2Si_2O_8$ liquid from first-principles molecular dynamics. Geochim. Cosmochim. Acta 74, 5657–5671.

de Koker, N., Stixrude, L., 2009. Self-consistent thermodynamic description of silicate liquids, with application to shock melting of MgO periclase and $MgSiO_3$ perovskite. Geophys. J. Int. 178, 162–179.

de Koker, N., Stixrude, L., Karki, B.B., 2008. Thermodynamics, structure, dynamics, and freezing of Mg_2SiO_4 liquid at high pressure. Geochim. Cosmochim. Acta 72, 1427–1441, http://dx.doi.org/10.1016/j.gca.2007.12.019.

Fiquet, G., 2010. Melting of peridotite to 140 gigapascals. Science 329, 1516–1518.

Ghiorso, M.S., Hirschmann, M.M., Reiners, P.W., Kress, V.C., 2002. The pMELTS: a revision of MELTS for improved calculation of phase relations and major element partitioning related to partial melting of the mantle to 3 GPa. Geochem. Geophy. Geosyst. 3, http://dx.doi.org/10.1029/2001GC000217.

Hageman, V.B.M., Oonk, H.A.J., 1986. Liquid immiscibility in the SiO_2+MgO, SiO_2+SrO, SiO_2+LaO_3, and SiO_2+Y_2O_3 systems. Phys. Chem. Glasses 27, 194–198.

Haselton, H.T., Newton, R.C., 1980. Thermodynamics of pyrope-grossular garnets and their stabilities at high temperatures and high pressures. J. Geophys. Res. 85, 697306982.

Hess, P.C., 1995. Thermodynamic mixing properties and the structure of silicate melts. In: Stebbins, J.F., McMillan, P.F., Dingwell, D.B. (Eds.), Structure, Dynamics and Properties of Silicate Melts. Mineralogical Society of America, Washington, D.C.

Hirose, K., Fei, Y., Ma, Y., Mao, H.K., 1999. The fate of subducted basaltic crust in the Earth's lower mantle. Nature 397, 53–56.

Hohenberg, P., Kohn, W., 1964. Inhomogeneous electron gas. Phys. Rev. B 136, B864.

Holland, K.G., Ahrens, T.J., 1997. Melting of $(Mg,Fe)_2SiO_4$ at the core–mantle boundary of the Earth. Science 275, 1623–1625.

Holland, T., Powell, R., 2003. Activity–composition relations for phases in petrological calculations: an asymmetric multicomponent formulation. Contrib. Mineral. Petrol 145, 492–501.

Hudon, P., Baker, D.R., 2002. The nature of phase separation in binary oxide melts and glasses. I. Silicate systems. J. Non-Cryst. Solids 303, 299–345.

Ito, E., Kubo, A., Katsura, T., Walter, M.J., 2004. Melting experiments of mantle materials under lower mantle conditions with implications for magma ocean differentiation. Phys. Earth Planet. Interiors 143–144, 397–406.

Jeanloz, R., Roufosse, M., 1982. Anharmonic properties—ionic model of the effects of compression and coordination change. J. Geophys. Res. 87, 763–772.

Karki, B., Stixrude, L., 2010. Viscosity of $MgSiO_3$ liquid at Earth's mantle conditions: implications for an early magma ocean. Science 238, 740–743.

Karki, B.B., Bhattarai, D., Stixrude, L., 2006. First principles calculations of the structural, dynamical and electronic properties of liquid MgO. Phys. Rev. B 73, 174208.

Karki, B.B., Bhattarai, D., Stixrude, L., 2007. First-principles simulations of liquid silica: structural and dynamical behavior at high pressure. Phys. Rev. B 76, 104205.

Ke, Y., Solomatov, V.S., 2006. Early transient superplumes and the origin of the Martian crustal dichotomy. J. Geophys. Res., 111, http://dx.doi.org/10.1029/2005JE002631.

Kohn, W., Sham, L.J., 1965. Self-consistent equations including exchange and correlation effects. Phys. Rev. 140, 1133.

Kresse, G., Furthmüller, J., 1996. Efficiency of ab-initio total energy calculations for metals and semiconductors using a plane-wave basis set. Comput. Mater. Sci. 6, 15–50.

Kresse, G., Hafner, J., 1994. Norm-conserving and ultrasoft pseudopotentials for first-row and transition-elements. J. Phys. Condens. Matter 6, 8245–8257.

Labrosse, S., Hernlund, J., Coltice, N., 2007. A crystallizing dense magma ocean at the base of the Earth's mantle. Nature 450, 866–869.

Lacks, D.J., Rear, D.B., Van Orman, J.A., 2007. Molecular dynamics investigation of viscosity, chemical diffusivities and partial molar volumes of liquids along the $MgO–SiO_2$ join as functions of pressure. Geochim. Cosmochim. Acta 71, 1312–1323.

Lange, R.A., 2007. The density and compressibility of $KAlSi_3O_8$ liquid to 6.5 GPa. Am. Mineral. 92, 114–123.

Lange, R.A., Carmichael, I.S.E., 1987. Densities of $Na_2O–K_2O–CaO–MgO–FeO–Fe_2O_3–Al_2O_3–TiO_2–SiO_2$ liquids—new measurements and derived partial molar properties. Geochim. Cosmochim. Acta 51, 2931–2946.

Martin, D., Nokes, R., 1989. A fluid-dynamical study of crystal settling in convecting magmas. J. Petrol. 30, 1471–1500.

McGahay, V., Tomozawa, M., 1989. The origin of phase separation in silicate melts and glasses. J. Non-Cryst. Solids 109, 27–34.

McQuarrie, D.A., 1984. Statistical Mechanics. University Science Books, Sausalito, CA.

Miller, G.H., Stolper, E.M., Ahrens, T.J., 1991. The equation of state of a molten Komatiite. 2. Application to Komatiite petrogenesis and the Hadean mantle. J. Geophys. Res. 96, 11849–11864.

Mosenfelder, J.L., Asimow, P.D., Ahrens, T.J., 2007. Thermodynamic properties of Mg_2SiO_4 liquid at ultra-high pressures from shock measurements to 200 GPa on forsterite and wadsleyite. J. Geophys. Res., 112, http://dx.doi.org/10.1029/2006JB004364.

Nomura, R., Ozawa, H., Tateno, S., Hirose, K., Hernlund, J., Muto, Y., Ishii, H., Hiraoka, N., 2011. Spin crossover and iron-rich silicate melt in the Earth's deep mantle. Nature 473, 199–202.

Oganov, A.R., Gillan, M., Price, G.D., 2005. Structural stability of silica at high pressures and temperatures. Phys. Rev. B 71, 064104.

Presnall, D.C., Weng, Y.-H., Milholland, C.S., Walter, M.J., 1998. Liquidus phase relations in the system $MgO–MgSiO_3$ at pressures up to 25 GPa—constraints on crystallization of a molten Hadean mantle. Phys. Earth Planet. Interiors 107, 83–95.

Riley, B., 1966. The Determination of melting points at temperatures above 2000° Celcius. Revue international des hautes temperatures et des refractaires 3, 327–336.

Solomatov, V.S., 2007. Magma oceans and primordial mantle differentiation. In: Schubert, G. (Ed.), Treatise on Geophysics, vol. 9. Evolution of the Earth. Elsevier, Amserdam.

Sparks, R.S.J., Huppert, H.E., Turner, J.S., 1984. The fluid dynamics of evolving magma chambers. Philos. Trans. R. Soc. London Ser. A 310, 511–534.

Stixrude, L., Bukowinski, M.S.T., 1990. A novel topological compression mechanism in a covalent liquid. Science 250, 541–543.

Stixrude, L., de Koker, N., Sun, N., Mookherjee, M., Karki, B.B., 2009. Thermodynamics of silicate liquids in the deep Earth. Earth Planet. Sci. Lett. 278, 226–232.

Stixrude, L., Karki, B., 2005. Structure and freezing of $MgSiO_3$ liquid in Earth's lower mantle. Science 310, 297–299.

Stixrude, L., Lithgow-Bertelloni, C., 2005. Thermodynamics of mantle minerals—I. Physical properties. Geophys. J. Int. 162, 610–632.

Sun, N., 2011. First principles molecular dynamics simulations of diopside ($CaMgSi_2O_6$) liquid to high pressure. Geochim. Cosmochim. Acta 75, 3792–3802.

Thompson Jr., J.B., 1967. Thermodynamic properties of simple solutions. Res. Geochem. 2, 340–361.

Trønnes, R.G., Frost, D.J., 2002. Peridotite melting and mineral-melt partitioning of major and minor elements at 22–24.5 GPa. Earth Planet. Sci. Lett. 197, 117–131.

Williams, Q., Garnero, E.J., 1996. Seismic evidence for partial melt at the base of Earth's mantle. Science 273, 1528–1530.

Zhou, Y., Miller, G.H., 1997. Constraints from molecular dynamics on the liquidus and solidus of the lower mantle. Geochim. Cosmochim. Acta 61, 2957–2976.

Supplimentary Online Material: Multi-Component Melting of Earth's Lowermost Mantle from First Principles

Nico de Koker, Bijaya Karki, Lars Stixrude

November 3, 2012

S1 Details of FPMD Simulations

The new intermediate compositions simulated are Mg_5SiO_7, $Mg_3Si_2O_7$, $MgSi_2O_5$, $MgSi_3O_7$, and $MgSi_5O_{11}$. Simulation cells have 78, 72, 72, 66, and 75 atoms, respectively. These intermediate systems are initiated by removing and/or transforming an appropriate number of atoms from either $MgSiO_3$ or Mg_2SiO_4 and evolving the resulting high energy configuration to a favorable state at 10000 K for at least 6000 time steps by FPMD; in all calculations in this work 1 time step = 1 femto second. Results obtained in test simulations initiated using geometries generated by classical molecular dynamics runs of 1 nano second differed negligibly from the FPMD production runs.

For compositions with no stable solid phases with which to compute the correction for the systematic overbinding in LDA, values are interpolated along the join using the known values for MgO, Mg_2SiO_4, $MgSiO_3$ and SiO_2 (Figure S1; Karki and Stixrude, 2010; de Koker and Stixrude, 2009; de Koker et al., 2008; Karki et al., 2007, 2006; Stixrude and Karki, 2005).

S2 Fundamental Thermodynamic Relations

S2.1 Description of Liquids

The liquid-state fundamental relation (LFTR) we use to model the thermodynamics of each simulated liquid composition was described in detail in de Koker and Stixrude (2009). The relation uses the Helmholtz free energy as thermodynamic potential, expressed as a function of its natural variables

$$F(V,T) = F_{\mathrm{ig}}(V,T) + F_{\mathrm{el}}(V,T) + F_{\mathrm{xs}}(V,T), \tag{S1}$$

by considering three separate contributions due to atomic momenta $F_{\mathrm{ig}}(V,T)$, electronic excitation $F_{\mathrm{el}}(V,T)$, and bonding $F_{\mathrm{xs}}(V,T)$, respectively.

$F_{\mathrm{xs}}(V,T)$ is written as a two-dimensional expansion in terms of functions $f(V)$ (Eulerian finite strain) and $\theta(T)$ about the reference volume and temperature V_0 and T_0,

$$F_{\mathrm{xs}}(V,T) = \sum_{i=0}^{\mathcal{O}'_f} \sum_{j=0}^{\mathcal{O}'_\theta} \frac{a_{ij}}{i!j!} f^i \theta^j; \tag{S2}$$

$$f = \frac{1}{2}\left[\left(\frac{V_0}{V}\right)^{\frac{2}{3}} - 1\right]; \qquad \theta = \left[\left(\frac{T}{T_0}\right)^m - 1\right]. \tag{S3}$$

$F_{\rm el}$ is given by

$$F_{\rm el}(V,T) = -\zeta\left[\frac{1}{2}\left(T^2 - T_{\rm el}^2\right) - TT_{\rm el}\ln\frac{T}{T_{\rm el}}\right], \tag{S4}$$

which follows by integration of the electronic heat capacity for a conductor, modified to account for the liquid being conductive only above $T_{\rm el}$, with ζ the electronic heat capacity coefficient. The volume dependence of ζ and $T_{\rm el}$ is described using power law relations

$$\zeta = \zeta_0\left(\frac{V}{V_0}\right)^{\xi}; \qquad T_{\rm el} = T_{\rm el0}\left(\frac{V}{V_0}\right)^{\eta}, \tag{S5}$$

with ζ_0, ξ, $T_{\rm el0}$, and η free parameters to be determined.

$F_{\rm ig}$ is the free energy of an ideal gas with a composition corresponding to that of the liquid (eg. Callen, 1985; McQuarrie, 1984)

$$F_{\rm ig}(V,T) = -k_{\rm B}T\sum_i N_i \ln\frac{eq_i}{N_i}, \tag{S6}$$

with the partition function

$$q_i = V\left(m_i k_{\rm B}/2\pi\hbar^2\right)^{3/2}, \tag{S7}$$

with m_i the atomic mass element i.

To obtain the level of accuracy in fitting of the LFTR to our FPMD results required for considering the thermodynamics of mixing, we use second order temperature fits ($\mathcal{O}_\theta = 2$). We find that MgO, Mg_5SiO_7, Mg_2SiO_4, $Mg_3Si_2O_7$, $MgSiO_3$, $MgSi_2O_5$, and $MgSi_3O_7$ are well fit by a third order finite strain expansion ($\mathcal{O}_f = 3$), while $MgSi_5O_{11}$ requires $\mathcal{O}_f = 4$, and SiO_2 $\mathcal{O}_f = 5$, consistent with our previous findings (de Koker and Stixrude, 2009). Fits for each composition are shown in Figures S2-S10, with thermodynamic properties at 0 GPa and 3000 K reported in Table 1 of the main text.

S2.2 Description of Solids

Thermodynamics of FPMD solids are described using the anharmonic relation for high T solids (SFTR) explained in de Koker and Stixrude (2009); for completeness we briefly summarize it here. The Helmholtz free energy of the solid is written as

$$F(V,T) = F(V_0,T_0) + F_{\rm cmp}(V,T_0) + F_{\rm th}(V,T), \tag{S8}$$

with $F(V_0,T_0)$ the free energy at reference volume V_0 and temperature T_0, $F_{\rm cmp}(V,T_0)$ the contribution due to isothermal compression, and $F_{\rm th}(V,T)$ that due to isochoric temperature differences relative to T_0.

F_{cmp} is expressed as an expansion in terms of the Eulerian finite strain (f) (Birch, 1952, 1978)

$$F_{\mathrm{cmp}} = 9K_{T0}V_0\left[\frac{1}{2}f^2 + \frac{1}{6}a_3 f^3 + \cdots\right], \tag{S9}$$

$$a_3 = 3\left(K'_{T0} - 4\right), \tag{S10}$$

V_0, K_{T0}, and K'_{T0} being the volume, bulk modulus, and its first pressure derivative at zero pressure and a reference temperature T_0.

F_{th} is obtained by integration of the entropy as

$$F_{\mathrm{th}}(V,T) = -S_0\left[T - T_0\right] - C_V\left[T\ln\frac{T}{T_0} - \left[T - T_0\right]\right] - C_V\left[T - T_0\right]\int_{V_0}^{V}\frac{\gamma(V',T_0)}{V'}dV', \tag{S11}$$

where S_0 is the entropy at zero pressure and reference temperature, C_V is the heat capacity at volume V, assumed to be constant as a function of T though not constrained to a harmonic value of $3Nk_{\mathrm{B}}$, and γ is the Grüneisen parameter, described as (Stixrude and Lithgow-Bertelloni, 2005)

$$\gamma = \frac{\gamma'_0 + \left(2\gamma'_0 + \gamma'_1\right)f + 2\gamma'_1 f^2}{3\left(2 + 2\gamma'_0 f + \gamma'_1 f^2\right)}, \tag{S12}$$

with

$$\gamma_0 = \frac{1}{6}\gamma'_0; \qquad q_0 = \frac{\gamma'_1 + 2\gamma'_0 - \gamma'^2_0}{-3\gamma'_0}. \tag{S13}$$

For MgO periclase, Mg_2SiO_4 forsterite, $MgSiO_3$ perovskite, and SiO_2 stishovite we use a third order finite strain expansion for F_{cmp}. Fits for each solid composition considered are shown in Figures S11-S14.

S3 Constraining Reference Entropy Values for Thermodynamic Relations of Simulated Phases

Complete description of the free energy in the liquid and solid fundamental relations requires the entropy at one reference point for each system to be known, i.e. 13 values of S_0 have to be specified, 9 for liquids and 4 for solids. Our description of the thermodynamics of mixing (eq. 2) gives the total entropy along the binary at constant P and T as

$$S = YS_{\mathrm{SiO_2}} + (1-Y)S_{\mathrm{MgO}} + S_{\mathrm{ideal}} + W'_{\mathrm{A}}Y^2(1-Y) + W'_{\mathrm{B}}(1-Y)^2Y, \tag{S14}$$

with

$$S_{\mathrm{ideal}} = R[Y\ln Y + (1-Y)\ln(1-Y)], \tag{S15}$$

$$Y = X/(X + \lambda(1 - X)), \tag{S16}$$

$$W' = -(\partial W/\partial T)_P. \tag{S17}$$

Constraining S_0 for the 9 liquid compositions therefore requires λ, W'_A, W'_B, $S_{\mathrm{SiO_2}}$, and S_MgO to be specified at a single chosen reference state, the P and T dependence of these quantities being fixed by our FPMD simulations. λ is determined from fitting to H_mix (Figure 1). W'_A and W'_B are constrained by optimizing with respect to three invariant points on the MgO–SiO_2 phase diagram (Figure S15) associated with the ambient pressure liquidi for periclase and forsterite together with the liquid immiscibility field. The three invariant points are i) the critical temperature of liquid immiscibility (T = 2250 K, X = 0.87; Hageman and Oonk, 1986), ii) the forsterite-periclase eutectic (T = 2136 K; X = 0.30 Bowen and Andersen, 1914), and iii) the forsterite-clinoenstatite peritectic (T_liquidus = 1830; X = 0.52 Bowen and Andersen, 1914). Values for $S_{\mathrm{SiO_2}}$ and S_MgO are chosen to optimize agreement with the available estimates of liquid entropy along the binary (Figure S16), obtained as

$$S_\mathrm{liq}(T, P) = S_\mathrm{sol}(T_\mathrm{m}, P) + \Delta S_\mathrm{m}(P) + \Delta S_\mathrm{liq}(T_\mathrm{m} \rightarrow T, P), \tag{S18}$$

where $\Delta S_\mathrm{liq}(T_\mathrm{m} \rightarrow T, P) = C_P \ln(T/T_\mathrm{m})$, and the subscript m indicates melting.

To constrain S_0 values in the crystalline phases in a manner that is consistent with the liquid entropies through their measured melting temperatures, we constrain the crystalline S_0 values by matching liquid Gibbs free energies at chosen experimental melting points. These fixed points are: 3070 K, 0 GPa for periclase (Riley, 1966); 2163 K, 0 GPa for forsterite (Bowen and Andersen, 1914); 2900 K, 25 GPa for perovskite (Stixrude and Karki, 2005, and references therein); 3120 K, 14 GPa for stishovite (Zhang et al., 1993; Shen and Lazor, 1995). Entropy values in our SFTRs are therefore not directly constrained from calorimetry data; a comparison between experimental entropy values and the values in our description is made in Table S1.

Our computed ambient pressure phase diagram agrees very well with the experimental data. The optimal S_mix model gives the periclase-forsterite eutectic at X = 0.31, T = 2136 K, and the forsterite-clinoenstatite peritectic at X = 0.52. We further obtain the critical point of immiscibility at T = 2250 K, X = 0.92, although our computed immiscibility field is narrower than the experimental curve. We find that the shape of the computed immiscibility field is sensitive to H_mix, but not to S_mix. Using a different mixing model will not increase the width of the field width, and the discrepancy likely results from the approximations made in treating the exchange-correlation energy at the first-principles level.

S4 Estimating the Influence of FeO

We estimate the influence of the addition of FeO on our results as

$$\mu_\alpha^\beta(X^*, Z) = \mu_\alpha^\beta(X^*) + RT \ln \gamma^\beta Z, \tag{S19}$$

where μ_α^β is the chemical potential of component α in phase β, γ is the activity coefficient, and the compositional variables

$$X^* = \frac{N_{\mathrm{SiO_2}}}{N_{\mathrm{SiO_2}} + N_{\mathrm{MgO}} + N_{\mathrm{FeO}}}, \tag{S20}$$

$$Z = \frac{N_{\mathrm{MgO}}}{N_{\mathrm{MgO}} + N_{\mathrm{FeO}}}. \tag{S21}$$

Motivated by the expectation that Fe will substitute primarily for Mg, we assume that

$$\mu_\alpha^\beta(X^*) = \mu_\alpha^\beta(X), \tag{S22}$$

where

$$X = \frac{N_{\mathrm{SiO_2}}}{N_{\mathrm{SiO_2}} + N_{\mathrm{MgO}}}. \tag{S23}$$

From our FPMD results, we know the first term on the right-hand side of eq. S19 for the components in the liquid phase (Lq), and for the solid phases stishovite (St) (or seifertite), ferropericlase (Fp) and perovskite (Pv) for which $\mu_\alpha^\beta(X^*)$ is simply the chemical potential of the pure end-member in the MgO-SiO_2 system. We can then find the influence of the FeO component on the phase diagram by equating chemical potentials in coexisting phases. In order to specify the solution completely, we further assume values of the Mg-Fe partition coefficients for the pairs liquid-ferropericlase and perovskite-ferropericlase. The system of equations to be solved is then

$$\begin{aligned}
\mu_{\mathrm{MgO}}^{\mathrm{Lq}}(X^*, Z) &= \mu_{\mathrm{MgO}}^{\mathrm{Fp}} + RT \ln \frac{Z^{\mathrm{Fp}}}{Z^{\mathrm{Lq}}}, && \text{(S24)}\\
\mu_{\mathrm{MgSiO_3}}^{\mathrm{Lq}}(X^*, Z) &= \mu_{\mathrm{MgSiO_3}}^{\mathrm{Pv}} + RT \ln \frac{Z^{\mathrm{Pv}}}{Z^{\mathrm{Lq}}}, && \text{(S25)}\\
\mu_{\mathrm{SiO_2}}^{\mathrm{Lq}}(X^*, Z) &= \mu_{\mathrm{SiO_2}}^{\mathrm{Pv}}, && \text{(S26)}\\
K^{\text{Lq-Fp}} &= \frac{Z^{\mathrm{Lq}}(1 - Z^{\mathrm{Fp}})}{Z^{\mathrm{Fp}}(1 - Z^{\mathrm{Lq}})}, && \text{(S27)}\\
K^{\text{Pv-Fp}} &= \frac{Z^{\mathrm{Pv}}(1 - Z^{\mathrm{Fp}})}{Z^{\mathrm{Fp}}(1 - Z^{\mathrm{Pv}})}, && \text{(S28)}
\end{aligned}$$

where $K^{\beta\text{-}\delta}$ is the Mg-Fe partition coefficient between phases β and δ, and we have further assumed that ratios of activity coefficients, e.g. $\gamma^{\mathrm{Pv}}/\gamma^{\mathrm{Lq}} \approx 1$ because Mg-Fe solution is found to be close to ideal in many silicate and oxide systems (eg. Stixrude and Lithgow-Bertelloni, 2011, and references therein). For example, for a given value of temperature T and Z^{Fp} of the bulk system, we may solve eqs. S24 and S27 for X^*, the silica fraction on the liquidus in the FeO-bearing system, along which $Z^{\mathrm{Lq}} = Z^{\mathrm{Fp}}$.

References

Alfè D. (2005) Melting curve of MgO from first-principles simulations. *Physical Review Letters* **94**, 235701.

Birch F. (1952) Elasticity and Constitution of the Earth's Interior. *Journal of Geophysical Research* **57**, 227–286.

Birch F. (1978) Finite Strain Isotherm and Velocities for Single-Crystal and Polycrystalline NaCl at High Pressures and 300 K. *Journal of Geophysical Research* **83**, 1257–1268.

Bowen N.L. and Andersen O. (1914) The binary system $MgO - SiO_2$. *American Journal of Science* **37**, 487–500.

Callen H.B. (1985) *Thermodynamics and an Introduction to Thermostatistics*. John Wiley & Sons, New York, 2nd edition.

de Koker N. and Stixrude L. (2009) Self-Consistent Thermodynamic Description of Silicate Liquids, with Application to Shock Melting of MgO Periclase and $MgSiO_3$ Perovskite. *Geophysical Journal International* **178**, 162–179.

de Koker N., Stixrude L. and Karki B.B. (2008) Thermodynamics, Structure, Dynamics, and Freezing of Mg_2SiO_4 Liquid at High Pressure. *Geochimica et Cosmochimica Acta* **72**, 1427–1441, doi:10.1016/j.gca.2007.12.019.

Ferguson J.B. and Merwin H.E. (1918) The Melting Points of Cristobalite and Tridymite. *American Journal of Science* **46**, 417–426.

Ghiorso M.S. and Carmichael I. (1980) A Regular Solution Model for Met-Aluminous Silicate Liquids: Applications to Geothermometry, Immiscibility, and the Source Regions of Basic Magmas. *Contributions to Mineralogy and Petrology* **71**, 323–342.

Hageman V.B.M. and Oonk H.A.J. (1986) Liquid immiscibility in the $SiO_2 + MgO$, $SiO_2 + SrO$, $SiO_2 + LaO_3$, and $SiO_2 + Y_2O_3$ systems. *Physics and Chemistry of Glasses* **27**, 194–198.

Hudon P., Jung I.H. and Baker D.R. (2002) Melting of β-quartz up to 2.0 GPa and thermodynamic optimization of the silica liquidus up to 6.0 GPa. *Physics of the Earth and Planetary Interiors* **130**, 159–174.

Karki B.B., Bhattarai D. and Stixrude L. (2006) First principles calculations of the structural, dynamical and electronic properties of liquid MgO. *Physical Review B* **73**, 174208.

Karki B.B., Bhattarai D. and Stixrude L. (2007) First-principles simulations of liquid silica: Structural and dynamical behavior at high pressure. *Physical Review B* **76**, 104205.

Karki B.B. and Stixrude L. (2010) First-principles study of enhancement of transport properties of silica melt by water. *Physical Review Letters* **104**, 215901.

McQuarrie D.A. (1984) *Statistical Mechanics*. University Science Books, Sausalito, CA.

Navrotsky A., Ziegler D., Oestrike R. and Maniar P. (1989) Calorimetry of Silicate Melts at 1773 K - Measurement of Enthalpies of Fusion and of Mixing in the Systems Diopside-Anorthite-Albite and Anorthite-Forsterite. *Contributions to Mineralogy and Petrology* **101**, 122–130.

Richet P., Bottinga Y., Denielou L., Petitet J.P. and Tequi C. (1982) Thermodynamic properties of quartz, cristobalite and amorphous SiO_2: drop calorimetry measurements between 1000 and 1800 K and a review from 0 to 2000 K. *Geochimica et Cosmochimica Acta* **46**, 2639–2658.

Riley B. (1966) The Determination of Melting Points at Temperatures Above 2000° Celcius. *Revue international des hautes temperatures et des refractaires* **3**, 327–336.

Robie R.A. and Hemingway B.S. (1995) *Thermodynamic Properties of Minerals and Related Substances at* 298.15 K *and* 1 Bar *(*10^5 Pascals*) Pressure and at Higher Temperatures*, volume 2131 of *USGS Bulletin*. Eastern Region, Reston, Va.

Shen G. and Lazor P. (1995) Measurement of melting temperatures of some minerals under lower mantle pressures. *Journal of Geophysical Research* **100**, 17699–17713.

Stebbins J.F., Carmichael I.S.E. and Moret L.K. (1984) Heat-Capacities and Entropies of Silicate Liquids and Glasses. *Contributions to Mineralogy and Petrology* **86**, 131–148.

Stixrude L. and Karki B.B. (2005) Structure and Freezing of $MgSiO_3$ liquid in the Earth's lower mantle. *Science* **310**, 297–299.

Stixrude L. and Lithgow-Bertelloni C. (2005) Thermodynamics of mantle minerals - I. Physical properties. *Geophysical Journal International* **162**, 610–632.

Stixrude L. and Lithgow-Bertelloni C. (2011) Thermodynamics of mantle minerals - II. Phase equilibria. *Geophysical Journal International* **in press**.

Tangeman J.A., Phillips B.L., Navrotsky A., Weber J.K.R., Hixson A.D. and Key T.S. (2001) Vitreous forsterite (Mg_2SiO_4): Synthesis, structure, and thermochemistry. *Geophysical Research Letters* **28**, 2517–2520.

Zhang J., Liebermann R.C., Gasparik T. and Herzberg C.T. (1993) Melting and Subsolidus Relations of SiO_2 at $9 - 14$ GPa. *Journal of Geophysical Research* **98**, 19785–19793.

Tables

Table S1: Entropy of FPMD simulated solid phases at the respective fixed melting points used to constrain their free energy by matching to liquid values.

	Periclase MgO	Forsterite Mg_2SiO_4	Perovskite $MgSiO_3$	Stishovite SiO_2
P (GPa)	0	0	25	14
T (Kelvin)	3070	2163	2900	3120
S (J/mol K)	145.3 (2)	440.7 (5)	306.0 (3)	163.5 (2)
Previous estimates	144 (1)†	419 (2)†	308 (2)‡	178 (2)‡

† Robie and Hemingway (1995);

‡ Stixrude and Lithgow-Bertelloni (2011)

S199 Figures

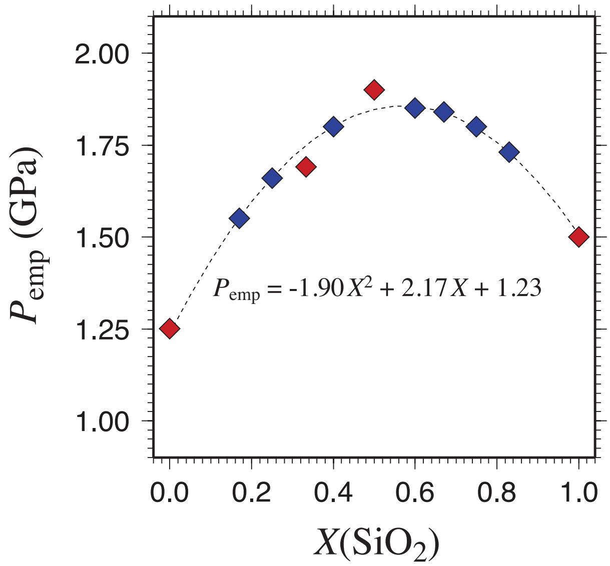

Figure S1: Interpolation of the pressure correction for systematic overbinding of LDA from phases for which it can be computed (red) to phases with no corresponding solid phases (blue).

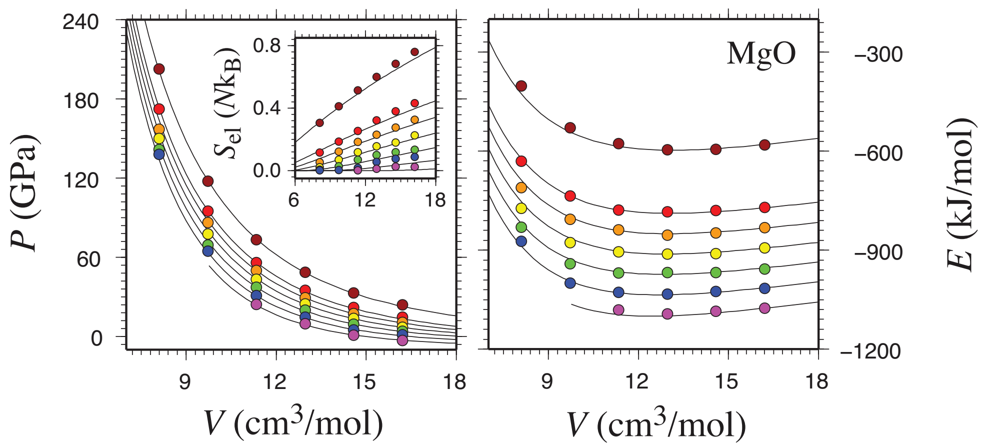

Figure S2: FPMD results (circles) and LFTR fit (lines) for MgO liquid. Purple - 2000 K; blue - 3000 K; green - 4000 K; yellow - 5000 K; orange - 6000 K; red - 7000 K; maroon - 10000 K.

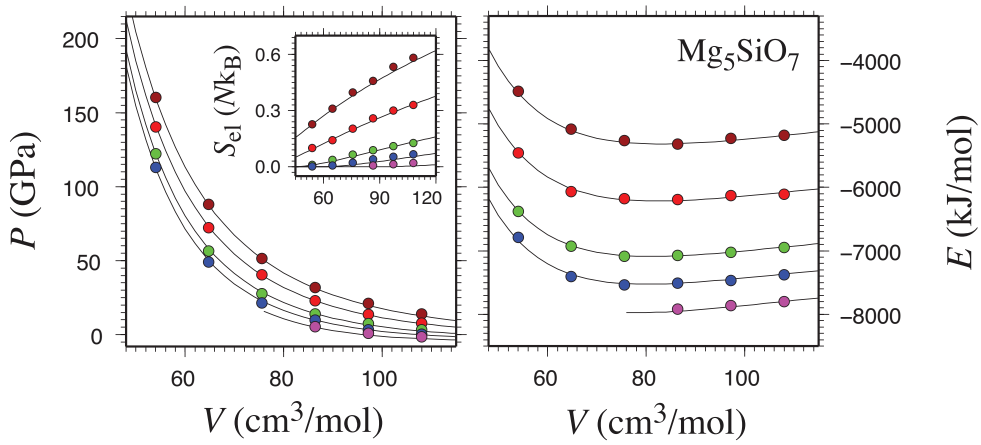

Figure S3: FPMD results (circles) and LFTR fit (lines) for Mg_5SiO_7 liquid. Purple - 2000 K; blue - 3000 K; green - 4000 K; red - 6000 K; maroon - 8000 K.

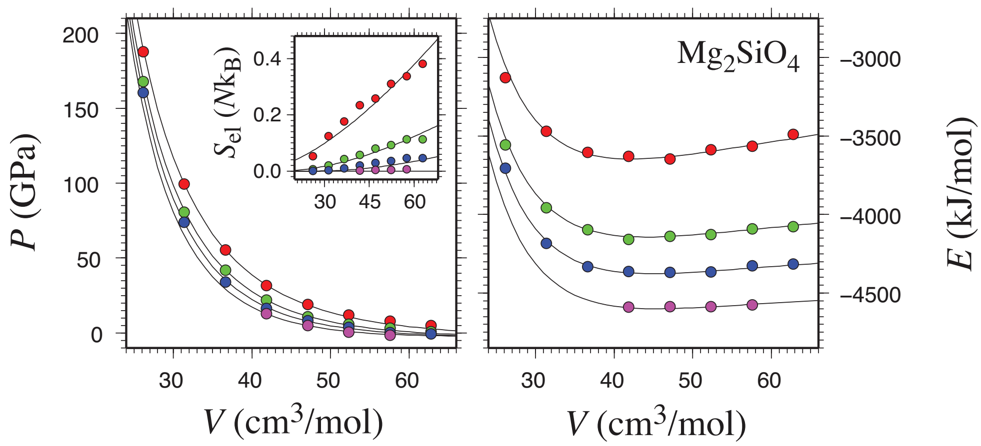

Figure S4: FPMD results (circles) and LFTR fit (lines) for Mg_2SiO_4 liquid. Purple - 2000 K; blue - 3000 K; green - 4000 K; red - 6000 K.

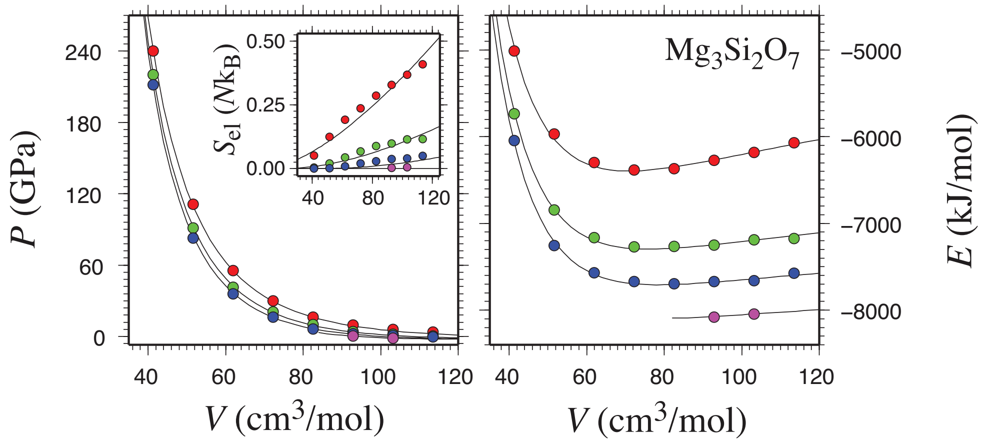

Figure S5: FPMD results (circles) and LFTR fit (lines) for $Mg_3Si_2O_7$ liquid. Purple - 2000 K; blue - 3000 K; green - 4000 K; red - 6000 K.

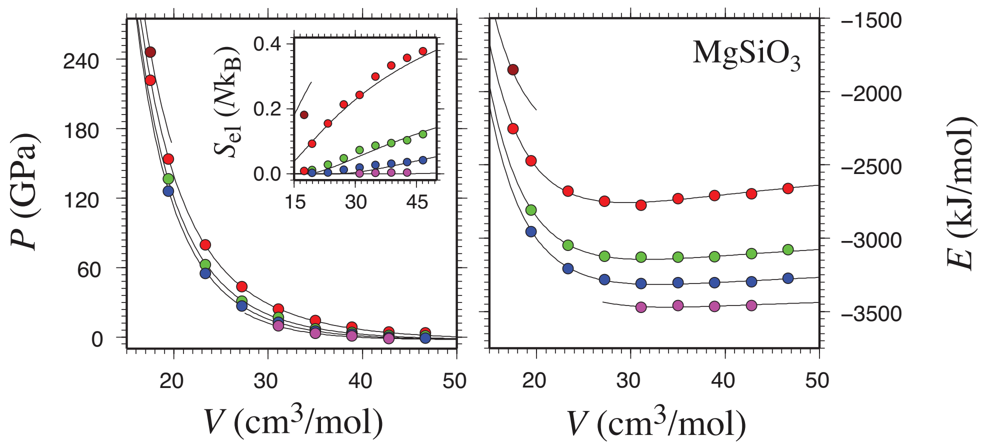

Figure S6: FPMD results (circles) and LFTR fit (lines) for $MgSiO_3$ liquid. Purple - 2000 K; blue - 3000 K; green - 4000 K; red - 6000 K; maroon - 8000 K.

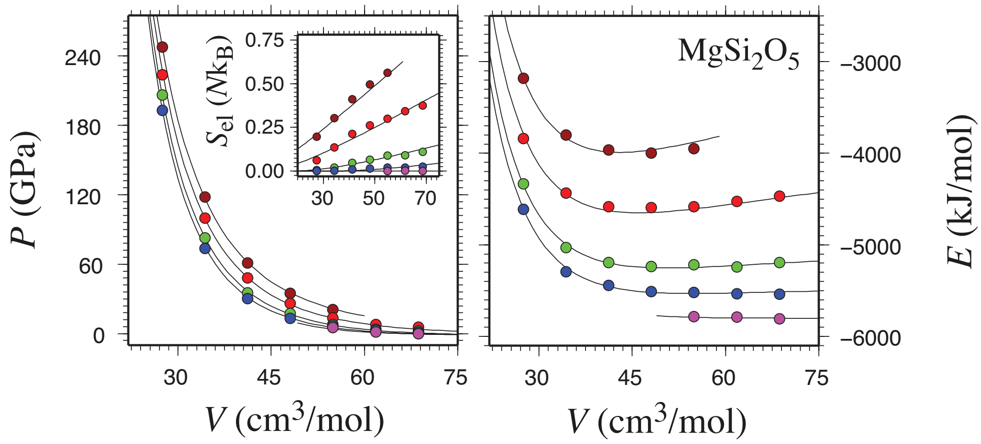

Figure S7: FPMD results (circles) and LFTR fit (lines) for $MgSi_2O_5$ liquid. Purple - 2000 K; blue - 3000 K; green - 4000 K; red - 6000 K; maroon - 8000 K.

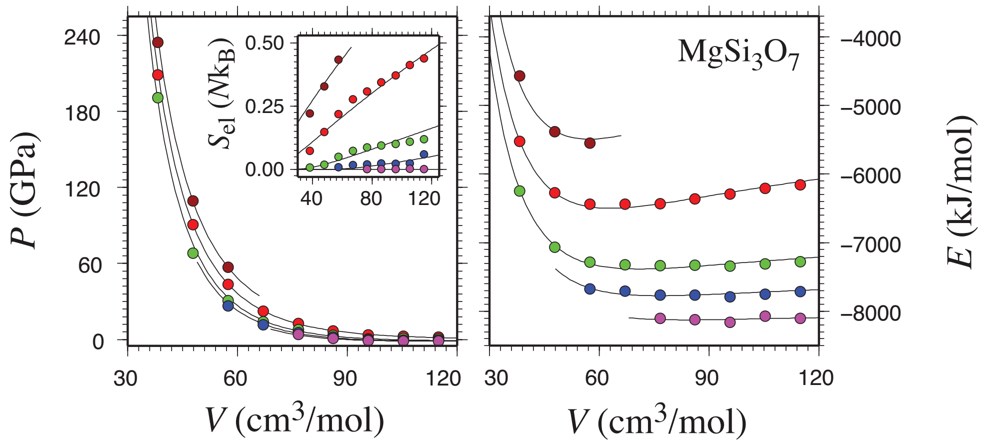

Figure S8: FPMD results (circles) and LFTR fit (lines) for $MgSi_3O_7$ liquid. Purple - 2000 K; blue - 3000 K; green - 4000 K; red - 6000 K; maroon - 8000 K.

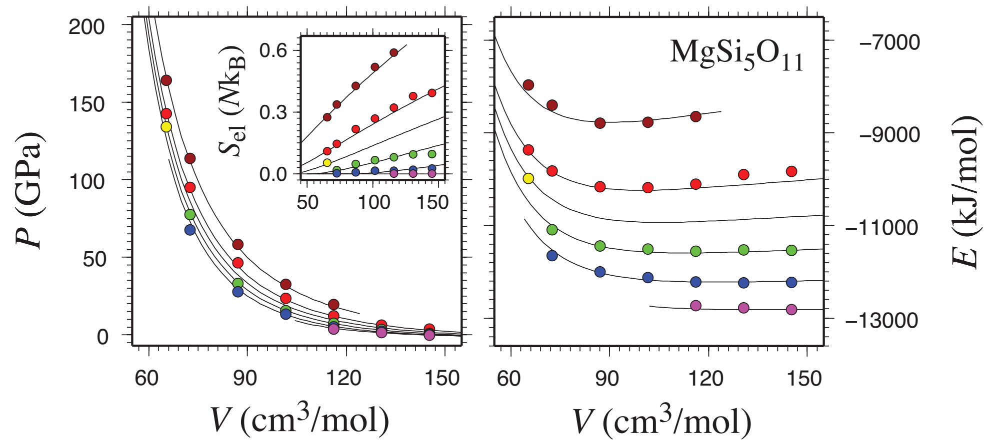

Figure S9: FPMD results (circles) and LFTR fit (lines) for $MgSi_5O_{11}$ liquid. Purple - 2000 K; blue - 3000 K; green - 4000 K; yellow - 5000 K; red - 6000 K; maroon - 8000 K.

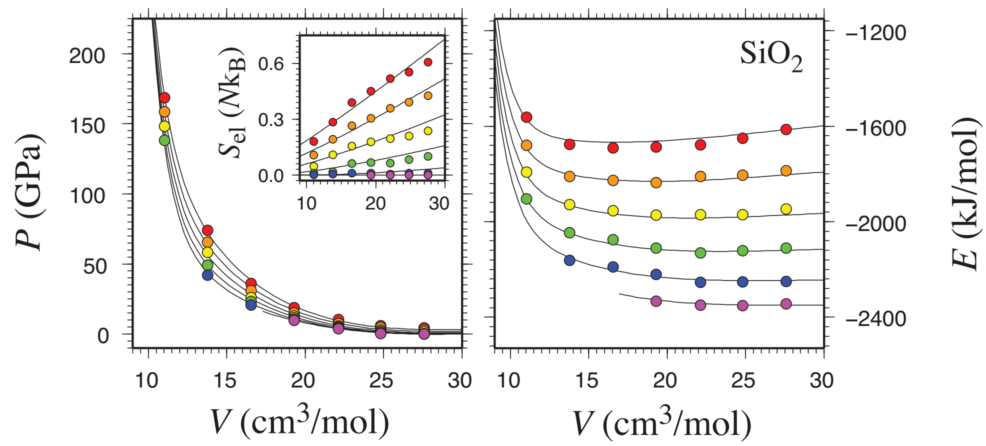

Figure S10: FPMD results (circles) and LFTR fit (lines) for SiO_2 liquid. Purple - 2000 K; blue - 3000 K; green - 4000 K; yellow - 5000 K; orange - 6000 K; red - 7000 K.

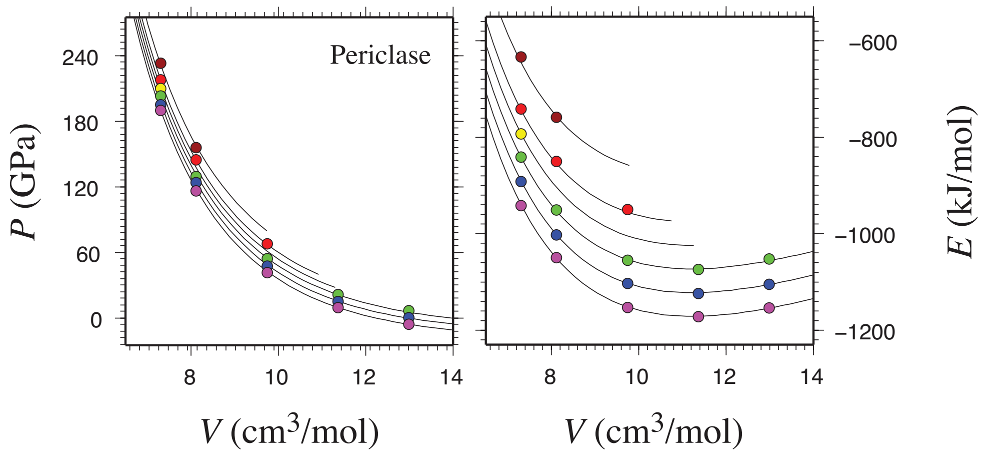

Figure S11: FPMD results (circles) and SFTR fit (lines) for MgO periclase. Purple - 2000 K; blue - 3000 K; green - 4000 K; yellow - 5000 K; red - 6000 K; maroon - 8000 K.

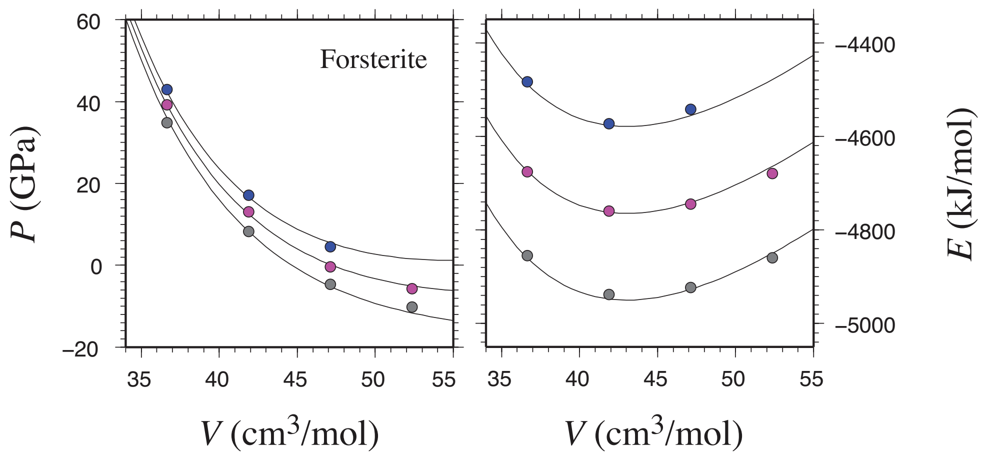

Figure S12: FPMD results (circles) and SFTR fit (lines) for Mg_2SiO_4 forsterite. Grey - 1000 K; purple - 2000 K; blue - 3000 K.

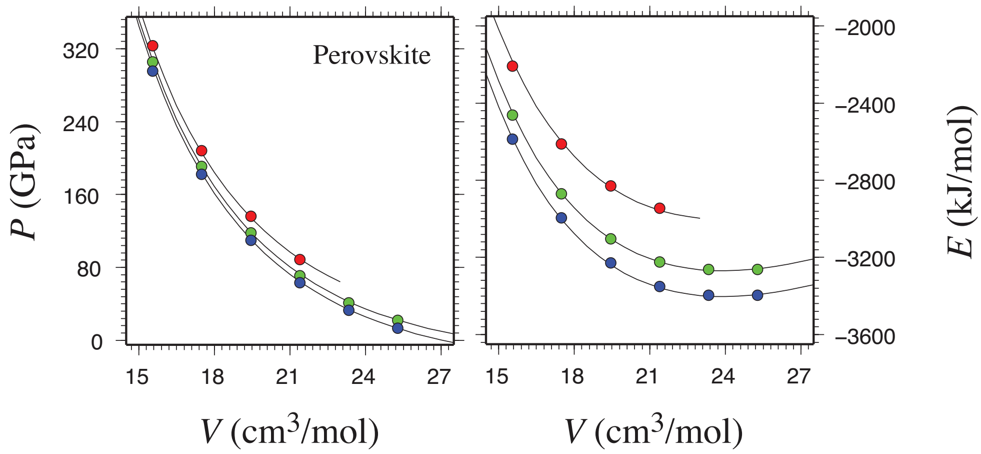

Figure S13: FPMD results (circles) and SFTR fit (lines) for $MgSiO_3$ perovskite. Blue - 3000 K; green - 4000 K; red - 6000 K.

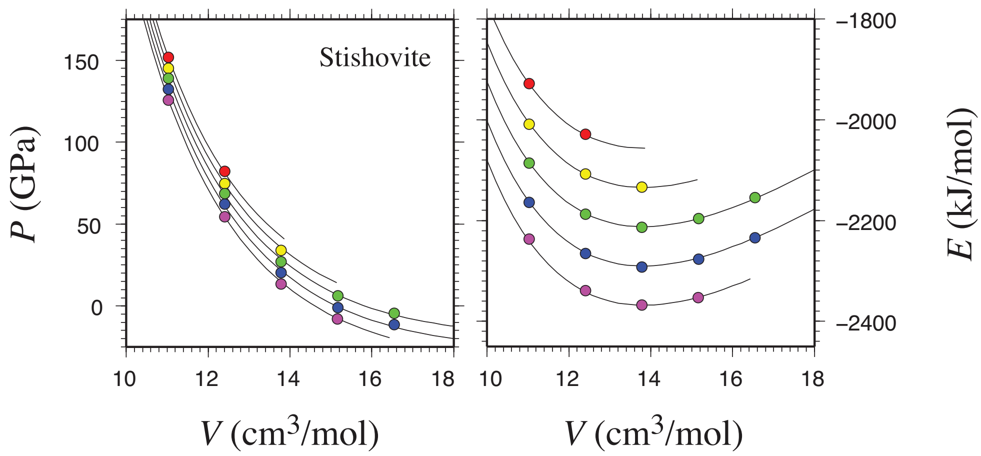

Figure S14: FPMD results (circles) and SFTR fit (lines) for SiO_2 stishovite. Purple - 2000 K; blue - 3000 K; green - 4000 K; yellow - 5000 K; red - 6000 K.

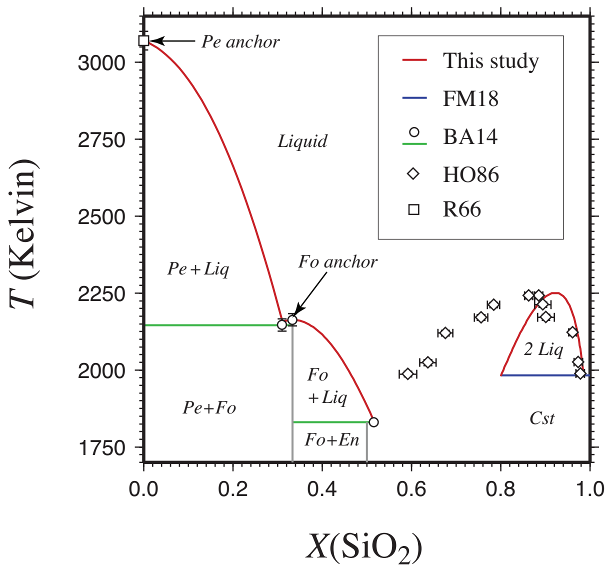

Figure S15: Ambient pressure phase equilibria used to constrain the reference entropy of mixing. Red curves are computed using our thermodynamic model; Liq - liquid, Pe - periclase, Fo - forsterite, En - enstatite, Cst - cristobalite; FM18 - Ferguson and Merwin (1918), BA14 - Bowen and Andersen (1914), HO86 - Hageman and Oonk (1986), R66 - Riley (1966). Points used to anchor free energies in thermodynamics models for periclase and forsterite are indicated (from left to right: periclase melting; periclase-forsterite eutectic; forsterite melting; forsterite+enstatite peritectic; liquid immiscibility field).

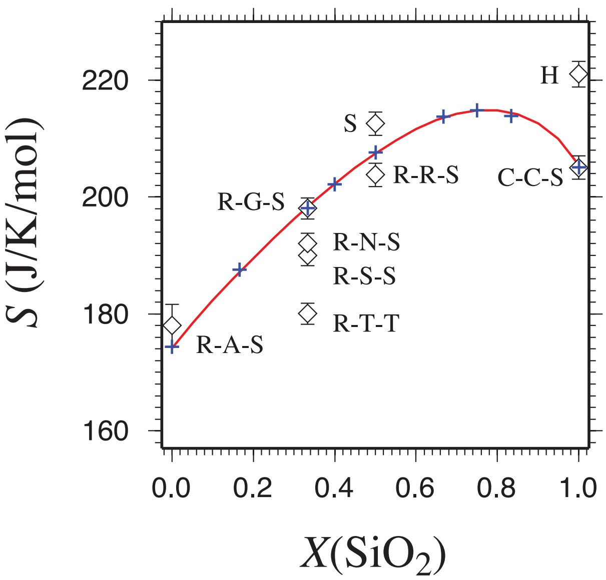

Figure S16: Reference third law entropy of the respective liquid compositions along the join (blue crosses) and the optimal entropy of mixing (red line) at ambient pressure and 3000 K, constrained via eq. S18 by optimizing agreement with the available estimates of the entropy of individual compositions (diamonds). Except where a single letter is noted, labels list the references used for the various components of eq. S18: $[S_{\rm sol}(T_{\rm m}, P)]$–$[\Delta S_{\rm fus}(P)]$–$[\Delta S_{\rm liq}(T_{\rm m} \rightarrow T, P)]$. Labels are: A - Alfè (2005), C - Richet et al. (1982), G - Ghiorso and Carmichael (1980), H - Hudon et al. (2002), N - Navrotsky et al. (1989), R - Robie and Hemingway (1995), S - Stebbins et al. (1984), T - Tangeman et al. (2001). Unit is per mol of oxides.